Effect of Prandtl number on heat transport enhancement in Rayleigh-Bénard convection under geometrical confinement

Kai Leong Chong,[1] Sebastian Wagner,[2] Matthias Kaczorowski,[1]
Olga Shishkina,[2] and Ke-Qing Xia[1,*]
[1]*Department of Physics, The Chinese University of Hong Kong, Shatin, Hong Kong, China*
[2]*Max Planck Institute for Dynamics and Self-Organization, Am Fassberg 17, 37077 Göttingen, Germany*

(Received 5 September 2017; published 9 January 2018)

We study, using direct numerical simulations, the effect of geometrical confinement on heat transport and flow structure in Rayleigh-Bénard convection in fluids with different Prandtl numbers. Our simulations span over two decades of Prandtl number Pr, $0.1 \leqslant \mathrm{Pr} \leqslant 40$, with the Rayleigh number Ra fixed at 10^8. The width-to-height aspect ratio Γ spans between 0.025 and 0.25, while the length-to-height aspect ratio is fixed at one. We first find that for $\mathrm{Pr} \geqslant 0.5$, geometrical confinement can lead to a significant enhancement in heat transport as characterized by the Nusselt number Nu. For those cases, Nu is maximal at a certain $\Gamma = \Gamma_{\mathrm{opt}}$ and the maximal relative enhancement generally increases with Pr over the explored parameter range. As opposed to the situation of $\mathrm{Pr} \geqslant 0.5$, confinement-induced enhancement in Nu is not realized for smaller values of Pr, such as 0.1 and 0.2. The Pr dependence of the heat transport enhancement can be understood in its relation to the coverage area of the thermal plumes over the thermal boundary layer (BL) where larger coverage is observed for larger Pr due to a smaller thermal diffusivity. We further show that Γ_{opt} is closely related to the crossing of thermal and momentum BLs and find that Nu declines sharply when the thickness ratio of the thermal and momentum BLs exceeds a certain value of about one. In addition, through examining the temporally averaged flow fields and two-dimensional mode decomposition, it is found that for smaller Pr the large-scale circulation is robust against the geometrical confinement of the convection cell. We further found that Γ_{opt} exhibits a power-law relation with Pr as $\Gamma_{\mathrm{opt}} = 0.11\,\mathrm{Pr}^{-0.060\pm0.004}$. Together with the result $\Gamma_{\mathrm{opt}} = 29.37\,\mathrm{Ra}^{-0.31}$ found by Chong *et al.* [Phys. Rev. Lett. **115**, 264503 (2015)], our findings provide a more complete picture of the geometrical confinement.

DOI: 10.1103/PhysRevFluids.3.013501

I. INTRODUCTION

Thermally driven flows are ubiquitous phenomena in nature and industrial applications. Turbulent Rayleigh-Bénard (RB) convection in a fluid layer heated from below and cooled from above is the classical model for studying such phenomena. This model has been used to investigate important issues related to the heat transport and flow dynamics in a broad range of research fields, including astrophysics, geophysics, and engineering [1–5]. In the past decade, extensive studies of RB convection have been conducted using experimental, numerical, and theoretical approaches [6–9]. In RB convection, the control parameters that govern the turbulent flow are the Rayleigh number Ra and the Prandtl number Pr. In addition, the geometry of the container also plays an important role, in particular, the diameter-to-height aspect ratio Γ. Studies of RB

*kxia@cuhk.edu.hk

convection usually concern global heat transport across the system and also the problem of heat flow optimization. It is particularly important in passive thermal management, which is sometimes indispensable in industrial and engineering applications. Various methods to passively enhance heat transport have been found in RB studies. For instance, in RB cells with rough surfaces [10–14], heat transport can be enhanced significantly as the roughness modifies the thermal boundary layers, leading to more frequent emission of thermal plumes. Examples also include RB flows with polymer additives [15–19]. Furthermore, heat transport can also be enhanced by adding a stabilizing force in addition to thermal driving such that highly coherent thermal plumes are formed [20–23].

Many of the studies on RB convection in the past decade [20,22–30] have been devoted to the investigation of how varying the geometrical control parameter can influence heat transport and flow properties. These can be separated into two categories: One with an aspect ratio larger than one and the other with the aspect ratio smaller than one. The present study focuses on the latter situation, i.e., RB convection under geometrical confinement. Huang *et al.* [20] have found that for a RB cell with $\mathrm{Pr} = 4.3$, the Nusselt number Nu can increase on decreasing the width-to-height aspect ratio Γ, while the flow strength is reduced monotonically at the same time. The numerical work by Chong *et al.* [22] has further extended the study to a much expanded range of parameters of $1/64 \leqslant \Gamma \leqslant 1$ and $10^7 \leqslant \mathrm{Ra} \leqslant 10^{10}$, at fixed $\mathrm{Pr} = 4.38$. They have discovered that the confinement-induced heat transport enhancement only occurs over a particular range of Γ for a given Ra. For weakly confined geometry, Nu is found to be insensitive to the decrease in Γ until the cell width becomes smaller than the average spacing between the thermal plumes near the thermal boundary layers. In other words, there exists an onset aspect ratio for enhancement which is found to as $\Gamma_c = 12.42\,\mathrm{Ra}^{-0.21}$ [22]. When Γ is below the onset value, the so-called plume-controlled regime sets in. Within this regime thermal plumes condensate into giant (or super) plumes at the opposite boundary layers, which enables them to more efficiently cool down or heat up the corresponding plate. In this regime, Nu increases continuously on decreasing Γ until the severely confined regime is entered [30]. The boundary between the two regimes suggests an optimal aspect ratio at which Nu is maximized and the dependence of Γ_{opt} on Ra is given by $\Gamma_{\mathrm{opt}} = 29.37\,\mathrm{Ra}^{-0.31}$. On the other hand, the study by Wagner and Shishkina [29] revealed that the existence of the plume-controlled regime depends strongly on Pr, as well as Ra. For example, for $\mathrm{Pr} = 0.786$ with $1/10 \leqslant \Gamma \leqslant 1$ and $10^5 \leqslant \mathrm{Ra} \leqslant 10^7$, no significant enhancement in Nu was found. All this calls for an in-depth study on the influence of Pr on confinement-induced Nu enhancement. Another issue to be studied is the flow dynamics, which depends strongly on the geometrical control parameters. For a convection cell with an aspect ratio around one, it is known that there exists a persistent large-scale circulation (LSC) of a single-roll flow pattern [31–34]. When the aspect ratio becomes much larger than one, the LSC turns into horizontally adjacent multiple rolls [26,35–37]. In contrast, LSC becomes unstable when the aspect ratio is reduced to less than one, as reflected by the increased flow reversals or cessations, for both three-dimensional [38,39] and quasi-two-dimensional configurations [40,41].

In this paper we present a comprehensive direct numerical simulation (DNS) study of the effect of Pr on heat transfer enhancement for RB convection under geometrical confinement. In addition to heat transport, we also analyze how Pr influences the confinement-induced change in global flow structures. The rest of the paper is organized as follows. In Sec. II we describe the numerical method and the simulation parameters. In Sec. III we first present the dependence of the global Nusselt number and Reynolds number on the aspect ratio for different Pr. Furthermore, an analysis on the local quantities, such as temperature fluctuations, velocity fluctuations, and boundary layer thickness, is presented. We then compare the global flow structures for different Pr and Γ, both qualitatively, via temporally averaged flow fields and quantitatively via two-dimensional (2D) mode decomposition. In Sec. IV we summarize our findings.

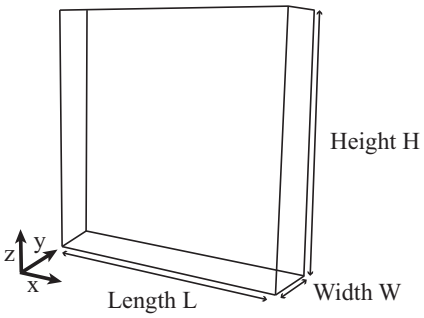

FIG. 1. Schematic diagram of the RB cell.

II. NUMERICAL METHODS AND SIMULATION PARAMETERS

The velocity field $\mathbf{u}$ is described by the Navier-Stokes equation within the Oberbeck-Boussinesq approximation together with the incompressibility condition. The temperature field T satisfies the advection-diffusion equation. The nondimensional form of these equations is given by

$$\partial \mathbf{u}/\partial t + \mathbf{u}\cdot\nabla\mathbf{u} + \nabla p = (\mathrm{Pr}/\mathrm{Ra})^{1/2}\nabla^2\mathbf{u} + \mathrm{T}\mathbf{z}, \tag{1}$$

$$\partial \mathrm{T}/\partial t + \mathbf{u}\cdot\nabla\mathrm{T} = (\mathrm{PrRa})^{-1/2}\nabla^2\mathrm{T}, \tag{2}$$

$$\nabla\cdot\mathbf{u} = 0, \tag{3}$$

where the dimensionless control parameters are the Rayleigh number $\mathrm{Ra} = \hat{\beta}\hat{g}\Delta\hat{T}\hat{H}^3/\hat{\nu}\hat{\kappa}$ and the Prandtl number $\mathrm{Pr} = \hat{\nu}/\hat{\kappa}$ (symbols with a circumflex represent dimensional parameters; those without a circumflex represent nondimensional parameters). Here $\hat{\beta}$, $\hat{\nu}$, and $\hat{\kappa}$ denote the thermal expansion coefficient, kinematic viscosity, and thermal diffusivity of the fluid and $\hat{g}$ is the gravitational acceleration pointing vertically. Also, $\Delta\hat{T} = \hat{T}_{\mathrm{bottom}} - \hat{T}_{\mathrm{top}}$ defines the temperature difference between the top and bottom plates separated by the cell height $\hat{H}$. The physical quantities are solved in dimensionless form, with the cell height $\hat{H}$ for the length scale and the free-fall time $(\hat{H}/\hat{\beta}\hat{g}\Delta\hat{T})^{1/2}$ for time scale, and the velocities are normalized by the free-fall velocity $(\hat{\beta}\hat{g}\Delta\hat{T}\hat{H})^{1/2}$. The temperature is made dimensionless by $T = (\hat{T} - \hat{T}_m)/\Delta\hat{T}$, with $\hat{T}_m = (\hat{T}_{\mathrm{bottom}} + \hat{T}_{\mathrm{top}})/2$ and $\hat{T}$ being the dimensional temperature. The DNSs are conducted in a box, presented in Fig. 1 together with the nomenclature and coordinates. For the domain boundaries, all walls are set to be nonslip and impermeable. The vertical walls are adiabatic, while the top and bottom plates are isothermal with $T_{\mathrm{top}} = -0.5$ and $T_{\mathrm{bottom}} = 0.5$ after normalization.

The equations are solved by a fourth-order finite-volume method on staggered grids. The Göttingen group used the GOLDFISH code as in Refs. [13,42], while the Hong Kong group used the CUPS code (Chinese University of Hong Kong Pencil Code simulation for turbulent convection), which is a well-tested extension [43,44] of the code [45]. A requirement for obtaining reliable results in DNS studies is to resolve the Kolmogorov (η_k) and the Batchelor (η_b) length scales. The global estimation of both scales in dimensionless form are given by $\eta_k = \sqrt{\mathrm{Pr}}/[\mathrm{Ra}(\mathrm{Nu}-1)]^{1/4}$ and $\eta_b = 1/[\mathrm{Ra}(\mathrm{Nu}-1)]^{1/4}$. From these relations we can see that the smallest length scale to be resolved for $\mathrm{Pr} > 1$ is η_b, whereas for $\mathrm{Pr} < 1$, η_k becomes the smallest scale. Also, sufficient resolution is needed inside the boundary layers, as suggested by Shishkina *et al.* [46], and thus a nonuniform mesh with denser grid points in the boundary layer regions is adopted in our simulations. Based on the above requirements, 768 vertical grid points were used for $\mathrm{Pr} = 0.1$ and 256 vertical grid points were used for $\mathrm{Pr} = 40$. The statistical data are collected after a statistical steady state has been reached as judged by the convergence of global Nu. Figure 2 shows examples of Nu time series after reaching a statistical steady state from where the oscillation about a certain mean value can be seen. We also notice that

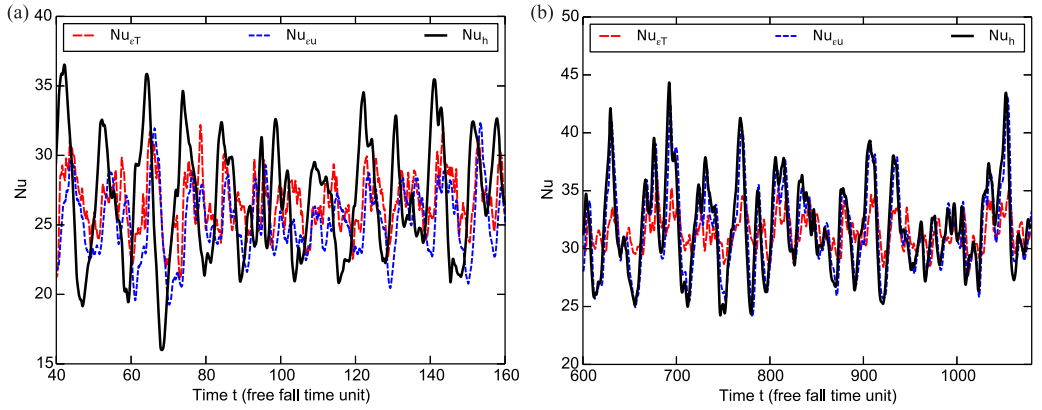

FIG. 2. Segment of Nusselt numbers versus time after reaching a statistical steady state for (a) $\mathrm{Pr} = 0.1$, $\Gamma = 0.25$, and $\mathrm{Ra} = 10^8$ and (b) $\mathrm{Pr} = 10$, $\Gamma = 0.25$, and $\mathrm{Ra} = 10^8$. Three different curves show the time series of the Nusselt number calculated by globally averaged viscous dissipation (Nu_{ϵ_u}), thermal dissipation (Nu_{ϵ_T}), and layer averaged heat flux (Nu_h), respectively. See the text for details.

the oscillation amplitudes of Nu depend on Pr. For small Pr, the oscillation amplitude of Nu_h is larger than that of Nu_{ϵ_u} and Nu_{ϵ_T}; for large Pr, Nu_{ϵ_u} almost coincides with Nu_h instantaneously, while the oscillation amplitude of Nu_{ϵ_T} is smaller than that of the other two. (The definitions of Nu_h, Nu_{ϵ_u} and Nu_{ϵ_T} are given below.)

We present simulations of 90 cases in total. To study how Pr affects heat transfer and flow dynamics with respect to geometrical confinement, over two decades of Pr ($0.1 \leqslant \mathrm{Pr} \leqslant 40$) have been covered and all fixed at the same Ra, which is 10^8. The width-to-height aspect ratio $\Gamma = W/H$ has been varied from 0.025 to 0.25 while the length-to-height aspect ratio was fixed at 1. The details of all the simulated cases including their meshes and check on the resolution requirements are summarized in Table I.

III. RESULTS AND DISCUSSION

A. Nusselt number and Reynolds number

We first examine the Nusselt number Nu and the Reynolds number Re. The evaluation of Nu is based on three different methods. The first one is to estimate global Nu through the formula $\mathrm{Nu}_h = \langle (\mathrm{Ra}\,\mathrm{Pr})^{1/2} u_z T - \partial T/\partial z \rangle_{x,y,t}$, where the symbol $\langle \cdot \rangle_{x,y,t}$ represents averaging over time and the entire horizontal plane. By taking the average of Nu_h across every horizontal plane, we can obtain the first estimation of Nu. Other ways to estimate Nu make use of the exact relations $\mathrm{Nu}_{\epsilon_u} = \langle \epsilon_u \rangle (\mathrm{Ra}\,\mathrm{Pr})^{1/2} + 1$ and $\mathrm{Nu}_{\epsilon_T} = \langle \epsilon_T \rangle (\mathrm{Ra}\,\mathrm{Pr})^{1/2}$, where $\langle \epsilon_u \rangle$ and $\langle \epsilon_T \rangle$ represent, respectively, the viscous and thermal dissipation rates averaged over time and the entire volume [47,48]. We obtain the numerically measured Nu by their mean value and the error of Nu is estimated by half of their standard deviation among Nu obtained with the three methods. The evaluation of Re is based on the formula $\mathrm{Re} = \sqrt{\langle \mathbf{u}^2 \rangle (\mathrm{Ra}/\mathrm{Pr})}$, where $\langle \mathbf{u}^2 \rangle$ represents the root-mean-square value of velocities averaged over time and the entire domain.

The Pr dependence of Nu for different values of Γ is shown in Fig. 3(a). For comparison, we also plot Nu as a function of Pr as estimated by Grossmann-Lohse (GL) theory with updated parameters [47,49] (shown as the black solid line). It can be seen that for $\Gamma = 0.25$ both the varying trend and the magnitude of Nu agree well with the GL theory. However, on decreasing Γ, the curves begin to deviate from the GL prediction since the effect of confinement sets in. According to Chong *et al.* [22], there exists an onset Γ above which the confinement effect is negligible. They have shown that the onset Γ is around 0.25 for $\mathrm{Ra} = 10^8$ and $\mathrm{Pr} = 4.38$ [see Fig. 1(a) in Ref. [22]].

TABLE I. Simulation parameters and the global convective heat flux (all at $\mathrm{Ra} = 10^8$). Columns from left to right indicate Pr, Γ, the number of grid points in the three spatial directions $N_z \times N_x \times N_y$, the averaged grid spacing in the vertical direction compared to the Kolmogorov length scale Δ_z/η_k (or to the Batchelor length scale Δ_z/η_b), the number of grid points in the thermal N_T and momentum N_u boundary layers (actual grid points and the requirement according to [46]), the averaging time t_{avg} in free-fall time units, the Nusselt number Nu, and the version of numerical code (GOLDFISH from the Göttingen group [13,42] or CUPS from the Hong Kong group [43,44]). For the evaluation of Nu and its error, we refer to Sec. III A.

Pr	Γ	$N_z \times N_x \times N_y$	Δ_z/η_k	Δ_z/η_b	N_T	N_u	t_{avg}	Nu	Code
0.1	0.025	$768 \times 768 \times 28$	0.77	0.24	40/2	20/1	200	13.36 ± 0.01	CUPS
	0.050	$768 \times 768 \times 42$	0.84	0.27	30/3	15/1	184	18.62 ± 0.06	CUPS
	0.075	$768 \times 768 \times 64$	0.87	0.27	27/3	13/1	184	20.83 ± 0.10	CUPS
	0.085	$768 \times 768 \times 68$	0.89	0.28	25/3	12/1	156	22.80 ± 0.12	CUPS
	0.100	$768 \times 768 \times 84$	0.90	0.28	24/3	12/2	144	23.72 ± 0.14	CUPS
	0.125	$768 \times 768 \times 100$	0.91	0.29	23/3	11/2	178	24.81 ± 0.19	CUPS
	0.150	$768 \times 768 \times 128$	0.91	0.29	23/3	11/2	178	25.11 ± 0.21	CUPS
	0.200	$768 \times 768 \times 168$	0.91	0.29	22/3	11/2	158	25.37 ± 0.26	CUPS
	0.250	$768 \times 768 \times 200$	0.92	0.29	22/3	11/2	141	26.14 ± 0.35	CUPS
0.2	0.025	$560 \times 560 \times 18$	0.75	0.34	28/2	17/1	200	13.78 ± 0.02	CUPS
	0.050	$560 \times 560 \times 32$	0.85	0.38	19/3	12/2	320	21.41 ± 0.04	CUPS
	0.075	$560 \times 560 \times 46$	0.89	0.40	16/3	10/2	320	25.49 ± 0.10	CUPS
	0.085	$560 \times 560 \times 52$	0.90	0.40	16/3	9/2	320	26.74 ± 0.12	CUPS
	0.100	$560 \times 560 \times 60$	0.91	0.41	15/4	9/2	320	27.95 ± 0.14	CUPS
	0.125	$560 \times 560 \times 74$	0.92	0.41	15/4	9/2	160	28.86 ± 0.17	CUPS
	0.150	$560 \times 560 \times 88$	0.91	0.41	15/4	9/2	320	28.15 ± 0.20	CUPS
	0.200	$560 \times 560 \times 116$	0.91	0.41	15/4	9/2	480	28.47 ± 0.22	CUPS
	0.250	$560 \times 560 \times 144$	0.91	0.41	15/4	9/2	160	28.35 ± 0.31	CUPS
0.5	0.025	$384 \times 512 \times 48$	0.71	0.50	29/3	24/2	674	14.90 ± 0.04	GOLDFISH
	0.050	$384 \times 512 \times 48$	0.81	0.57	20/3	16/3	1349	23.92 ± 0.05	GOLDFISH
	0.075	$384 \times 512 \times 74$	0.86	0.61	16/4	13/3	750	30.57 ± 0.06	GOLDFISH
	0.085	$384 \times 512 \times 78$	0.87	0.61	8/4	6/3	210	31.89 ± 0.08	CUPS
	0.100	$384 \times 512 \times 98$	0.88	0.62	15/4	12/3	880	32.87 ± 0.07	GOLDFISH
	0.125	$384 \times 512 \times 100$	0.87	0.62	15/4	12/3	564	32.70 ± 0.09	GOLDFISH
	0.150	$384 \times 512 \times 128$	0.87	0.62	15/4	12/3	681	32.58 ± 0.07	GOLDFISH
	0.200	$384 \times 512 \times 160$	0.87	0.61	15/4	12/3	588	31.75 ± 0.06	GOLDFISH
	0.250	$384 \times 512 \times 200$	0.86	0.61	16/4	13/3	473	31.22 ± 0.05	GOLDFISH
0.786	0.025	$384 \times 512 \times 48$	0.57	0.50	29/3	27/2	672	15.00 ± 0.03	GOLDFISH
	0.050	$384 \times 512 \times 48$	0.65	0.58	19/3	18/3	1336	24.83 ± 0.02	GOLDFISH
	0.075	$384 \times 512 \times 74$	0.70	0.62	15/4	14/4	739	32.74 ± 0.03	GOLDFISH
	0.085	$384 \times 512 \times 78$	0.70	0.62	8/4	7/4	210	33.39 ± 0.04	CUPS
	0.100	$384 \times 512 \times 98$	0.71	0.63	14/4	13/4	750	34.42 ± 0.06	GOLDFISH
	0.125	$384 \times 512 \times 100$	0.70	0.62	15/4	13/4	749	34.09 ± 0.06	GOLDFISH
	0.150	$384 \times 512 \times 128$	0.70	0.62	15/4	13/4	700	33.99 ± 0.06	GOLDFISH
	0.200	$384 \times 512 \times 160$	0.70	0.62	15/4	14/4	611	32.44 ± 0.03	GOLDFISH
	0.250	$320 \times 320 \times 96$	0.83	0.73	8/4	7/3	520	31.47 ± 0.06	CUPS
1	0.025	$384 \times 512 \times 48$	0.51	0.51	28/3	28/3	786	15.42 ± 0.03	GOLDFISH
	0.050	$384 \times 512 \times 48$	0.58	0.58	19/3	19/3	934	25.23 ± 0.05	GOLDFISH
	0.075	$384 \times 512 \times 74$	0.62	0.62	15/4	15/4	996	32.88 ± 0.04	GOLDFISH
	0.085	$384 \times 512 \times 78$	0.63	0.63	8/4	7/4	420	34.41 ± 0.08	CUPS
	0.100	$384 \times 512 \times 98$	0.63	0.63	14/4	14/4	972	35.15 ± 0.06	GOLDFISH
	0.125	$384 \times 512 \times 100$	0.63	0.63	14/4	14/4	817	34.83 ± 0.04	GOLDFISH
	0.150	$384 \times 512 \times 128$	0.62	0.62	15/4	14/4	748	34.10 ± 0.05	GOLDFISH
	0.200	$384 \times 512 \times 160$	0.62	0.62	15/4	15/4	707	32.90 ± 0.05	GOLDFISH

TABLE I. (*Continued.*)

Pr	Γ	$N_z \times N_x \times N_y$	Δ_z/η_k	Δ_z/η_b	N_T	N_u	t_{avg}	Nu	Code
	0.250	$384 \times 512 \times 200$	0.62	0.62	15/4	15/4	837	32.11 ± 0.05	GOLDFISH
2.5	0.025	$384 \times 512 \times 48$	0.33	0.52	26/3	33/4	1126	17.24 ± 0.01	GOLDFISH
	0.050	$384 \times 512 \times 48$	0.37	0.59	18/3	23/5	2000	27.42 ± 0.04	GOLDFISH
	0.075	$384 \times 512 \times 74$	0.39	0.62	15/4	19/5	989	33.79 ± 0.03	GOLDFISH
	0.085	$384 \times 512 \times 78$	0.40	0.63	7/4	9/5	420	35.51 ± 0.11	CUPS
	0.100	$384 \times 512 \times 98$	0.40	0.63	14/4	18/5	1086	35.73 ± 0.04	GOLDFISH
	0.125	$384 \times 512 \times 100$	0.40	0.63	14/4	18/5	1009	35.44 ± 0.03	GOLDFISH
	0.150	$384 \times 512 \times 128$	0.40	0.63	14/4	18/5	829	34.83 ± 0.04	GOLDFISH
	0.200	$384 \times 512 \times 160$	0.39	0.62	15/4	19/5	669	33.50 ± 0.04	GOLDFISH
	0.250	$384 \times 512 \times 200$	0.39	0.62	15/4	19/5	538	32.92 ± 0.04	GOLDFISH
4.38	0.025	$256 \times 256 \times 16$	0.38	0.80	11/3	16/5	300	18.35 ± 0.01	CUPS
	0.050	$256 \times 256 \times 20$	0.43	0.90	7/4	11/6	400	28.70 ± 0.08	CUPS
	0.075	$256 \times 256 \times 28$	0.45	0.93	9/4	13/6	500	33.51 ± 0.08	CUPS
	0.085	$256 \times 256 \times 28$	0.45	0.93	6/4	9/7	300	35.14 ± 0.11	CUPS
	0.100	$256 \times 256 \times 36$	0.45	0.95	6/4	9/7	640	35.41 ± 0.11	CUPS
	0.125	$256 \times 256 \times 38$	0.45	0.94	6/4	9/7	370	34.63 ± 0.18	CUPS
	0.150	$256 \times 256 \times 68$	0.45	0.94	9/4	13/6	350	34.13 ± 0.07	CUPS
	0.200	$256 \times 256 \times 68$	0.45	0.93	6/4	9/6	350	33.30 ± 0.08	CUPS
	0.250	$256 \times 256 \times 72$	0.44	0.92	7/4	10/6	380	32.20 ± 0.09	CUPS
10	0.025	$256 \times 256 \times 8$	0.17	0.53	20/3	36/6	413	18.41 ± 0.11	CUPS
	0.050	$256 \times 256 \times 16$	0.19	0.60	10/4	17/8	600	29.62 ± 0.07	CUPS
	0.075	$256 \times 256 \times 24$	0.20	0.63	9/4	16/9	510	34.26 ± 0.08	CUPS
	0.085	$256 \times 256 \times 24$	0.20	0.63	6/4	11/9	508	35.20 ± 0.12	CUPS
	0.100	$256 \times 256 \times 26$	0.20	0.63	8/4	14/9	375	34.98 ± 0.10	CUPS
	0.125	$256 \times 256 \times 26$	0.20	0.63	9/4	16/8	180	33.88 ± 0.04	CUPS
	0.150	$256 \times 256 \times 42$	0.20	0.62	9/4	16/8	345	32.85 ± 0.06	CUPS
	0.200	$256 \times 256 \times 60$	0.19	0.62	9/4	16/8	270	32.19 ± 0.08	CUPS
	0.250	$256 \times 256 \times 64$	0.19	0.61	9/4	16/8	560	31.65 ± 0.10	CUPS
20	0.025	$256 \times 256 \times 8$	0.18	0.81	12/3	27/8	490	18.82 ± 0.11	CUPS
	0.050	$256 \times 256 \times 16$	0.20	0.91	10/4	21/10	945	30.10 ± 0.04	CUPS
	0.075	$256 \times 256 \times 24$	0.21	0.95	9/4	18/11	751	35.25 ± 0.13	CUPS
	0.085	$256 \times 256 \times 24$	0.21	0.95	6/4	13/11	509	35.81 ± 0.12	CUPS
	0.100	$256 \times 256 \times 26$	0.21	0.95	7/4	16/11	375	35.53 ± 0.15	CUPS
	0.125	$256 \times 256 \times 34$	0.21	0.93	9/4	19/11	687	33.43 ± 0.05	CUPS
	0.150	$256 \times 256 \times 42$	0.21	0.92	9/4	20/10	728	32.09 ± 0.04	CUPS
	0.200	$256 \times 256 \times 60$	0.21	0.92	9/4	20/10	378	31.89 ± 0.02	CUPS
	0.250	$256 \times 256 \times 64$	0.21	0.92	9/4	19/10	300	31.19 ± 0.10	CUPS
40	0.025	$256 \times 256 \times 8$	0.13	0.81	12/3	32/10	875	19.40 ± 0.14	CUPS
	0.050	$256 \times 256 \times 16$	0.14	0.91	10/4	24/13	560	30.44 ± 0.05	CUPS
	0.075	$256 \times 256 \times 24$	0.15	0.95	9/4	22/14	952	35.75 ± 0.05	CUPS
	0.085	$256 \times 256 \times 24$	0.15	0.95	6/4	16/14	270	37.04 ± 0.05	CUPS
	0.100	$256 \times 256 \times 26$	0.15	0.95	7/4	20/14	1000	35.70 ± 0.05	CUPS
	0.125	$256 \times 256 \times 34$	0.15	0.94	9/4	23/13	700	33.71 ± 0.02	CUPS
	0.150	$256 \times 256 \times 42$	0.15	0.93	9/4	23/13	322	32.12 ± 0.06	CUPS
	0.200	$256 \times 256 \times 60$	0.15	0.92	9/4	24/13	504	31.37 ± 0.04	CUPS
	0.250	$256 \times 256 \times 64$	0.15	0.92	9/4	22/13	280	32.11 ± 0.16	CUPS

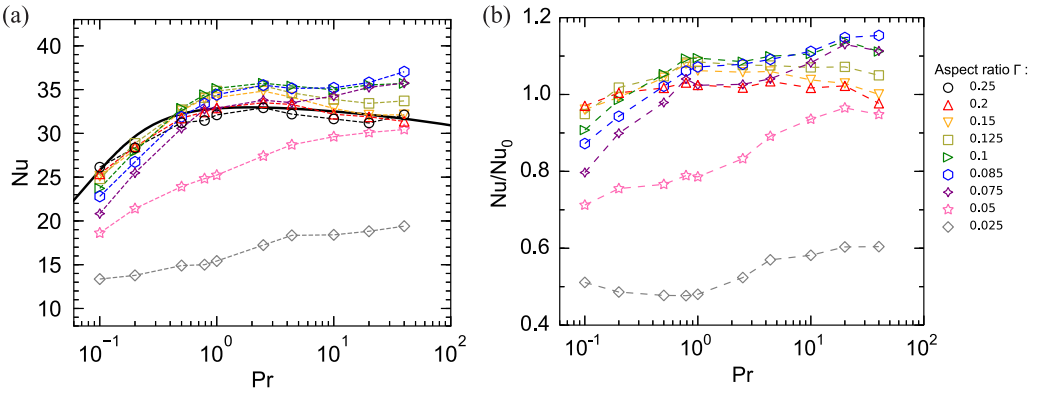

FIG. 3. (a) Global Nusselt number Nu and (b) normalized global Nusselt number versus Pr, for different Γ, where Nu_0 is the value obtained at $\Gamma = 0.25$. The black solid line is the Pr dependence of Nu estimated by Grossmann-Lohse theory [47,49].

Here, with different Pr explored, we further suggest that the cases of $\Gamma = 0.25$ can be regarded as a baseline representing unconfined RB convection according to their agreement with GL theory (at least within our explored Pr range). Another feature that can be seen in Fig. 3(a) is the weak Pr dependence of Nu for large Pr, which was also observed experimentally by Xia *et al.* [50]. Such a weak dependence has also been predicted by GL theory [51] and recently a numerical and theoretical work by Shishkina *et al.* [52] has even shown that Nu is totally independent of Pr for the regime of large Pr.

With the Nu value for $\Gamma = 0.25$ taken as the baseline for unconfined convection, we plot in Fig. 3(b) the normalized Nu versus Pr for the different values of Γ. In addition to showing the general trend that Nu increases with Pr in the present parameter range [which can also be seen in Fig. 3(a)], Fig. 3(b) also shows that, broadly speaking, upon geometrical confinement an enhancement in Nu sets in when $\mathrm{Pr} \gtrapprox 1$ and the enhancement increases with decreasing Γ up to a certain value. Then a sharp drop in Nu occurs.

Next we examine the enhancement effect in more detail by plotting the normalized Nu versus Γ for a given Pr, which is shown in Fig. 4(a). With this, the Pr dependence of the system's response to confinement can be classified as follows. The cases with $\mathrm{Pr} \geqslant 0.5$ appear to belong to one group, for which a regime with significant enhancement of Nu exists upon decreasing Γ. The cases with $\mathrm{Pr} = 0.1$ and 0.2 belong to the second group, for which no significant Nu enhancement is seen. We define "significant enhancement" as a more than 2% increase in Nu compared to Nu_0, which is about twice the maximum percentage error of Nu. We also find that the Reynolds number Re exhibits an apparent and monotonic decrease with Γ, as shown in Fig. 4(b). These results are in agreement with the previous finding that slower flow can indeed transport more heat [20]. For the cases with enhanced heat transport, Nu reaches a maximum value upon further confinement, after which heat transport efficiency declines sharply and the optimal aspect ratio Γ_{opt} can be defined through this trend.

Figure 4(c) shows the dependence of Γ_{opt} on Pr in a log-log plot. In order to estimate Γ_{opt} more accurately, a quadratic fit has been made to the three points in the neighborhood of the peak position in Fig. 4(a). The figure reveals that there is a power-law relationship between the two quantities and the fitting of respective data yields $\Gamma_{\mathrm{opt}} = 0.11\,\mathrm{Pr}^{-0.060\pm0.004}$. It is worthwhile to recall that the relationship between Γ_{opt} and Ra has been found previously [22], where Γ_{opt} and Ra follow a much stronger power-law relation $\Gamma_{\mathrm{opt}} = 29.37\,\mathrm{Ra}^{-0.31}$. In Fig. 4(d) we further examine the maximum enhancement versus Pr. The data are somewhat scattered, but a general trend is that the amount of enhancement increases with Pr within the explored parameter range. For instance, for $\mathrm{Pr} = 0.5$ the enhancement is ~5.3%, while for $\mathrm{Pr} = 40$ the enhancement is 15.3%.

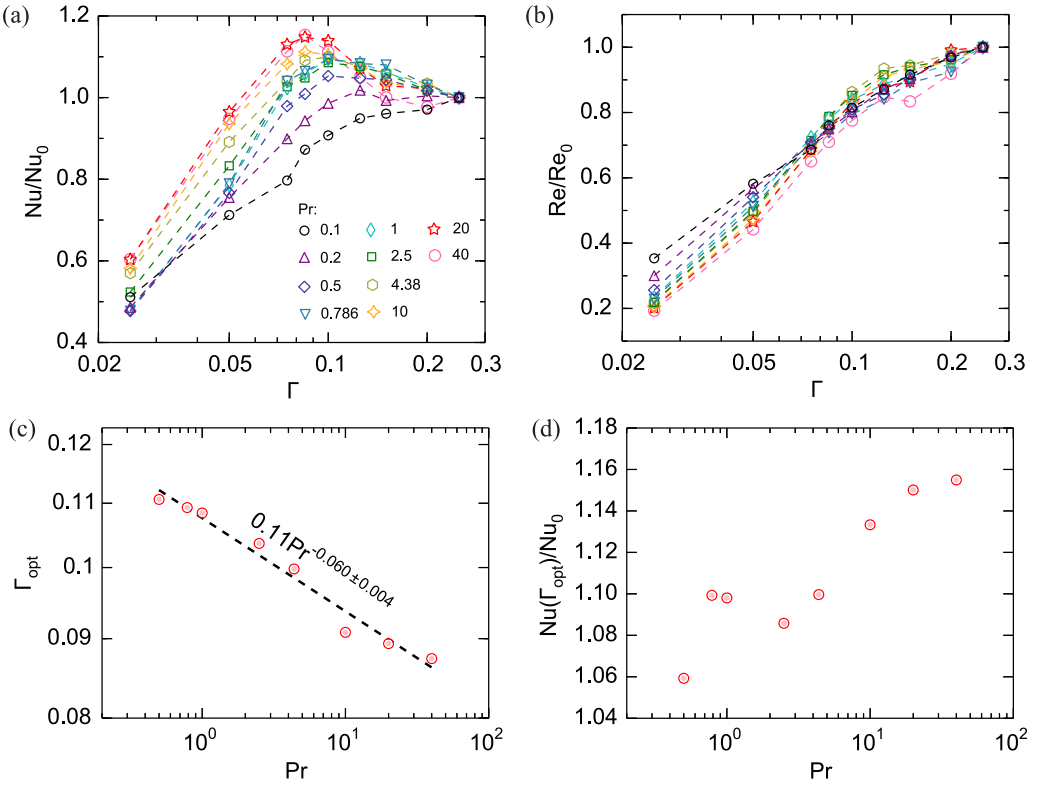

FIG. 4. Normalized (a) global Nusselt number and (b) Reynolds number versus Γ, for different Pr, where Nu_0 and Re_0 are the values obtained at $\Gamma = 0.25$. (c) Optimal aspect ratio Γ_{opt} (if it exists) versus Pr, where the dashed line represents the best power-law fit $\Gamma_{\mathrm{opt}} = 0.11\,\mathrm{Pr}^{-0.060\pm0.004}$. (d) Maximum Nu enhancement $\mathrm{Nu}(\Gamma_{\mathrm{opt}})/\mathrm{Nu}_0$ versus Pr.

B. Joint probability density function of velocity and temperature fluctuations

To gain further insight into how the bulk flow is modified by geometrical confinement, especially for fluid with different Pr, we now focus on the local quantities. One such local measurement that is able to reveal bulk flow properties is the joint probability density function between the temperature and vertical velocity at the midheight of the cell, which is shown in Fig. 5. The figure can be interpreted from two perspectives, either at fixed Γ with varying Pr or at fixed Pr with varying Γ. First, as Pr increases (from top to bottom along the columns), the shape of distribution function shrinks horizontally, meaning that for larger Pr the extreme events for velocity become less probable. This feature can be understood as the fluid flow becomes less turbulent for larger Pr, which is revealed by decreasing Re with increasing Pr. Second, as Γ decreases with fixed Pr (from left to right along the rows), the shape change of the distribution functions leads us to identify two competing effects. On the one hand, geometrical confinement slows down the bulk flow due to stronger drag from the sidewalls and hence it is less probable for large velocities to occur. On the other hand, confinement leads to the formation of highly coherent plumes [20] and thus the temperature distribution is elongated since hot (cold) plumes become hotter (colder) when they reach the midheight. However, the bulk properties observed here cannot explain why Nu enhancement has not been realized for $\mathrm{Pr} = 0.1$ and 0.2. As can be seen, increasing plume coherency in the bulk has also been realized for $\mathrm{Pr} = 0.1$, but in such case there is no heat transport enhancement globally. This observation suggests that instead of a bulk property, other quantities may also play important roles in heat transport enhancement, for example, the local properties at the edge of the boundary layer (BL).

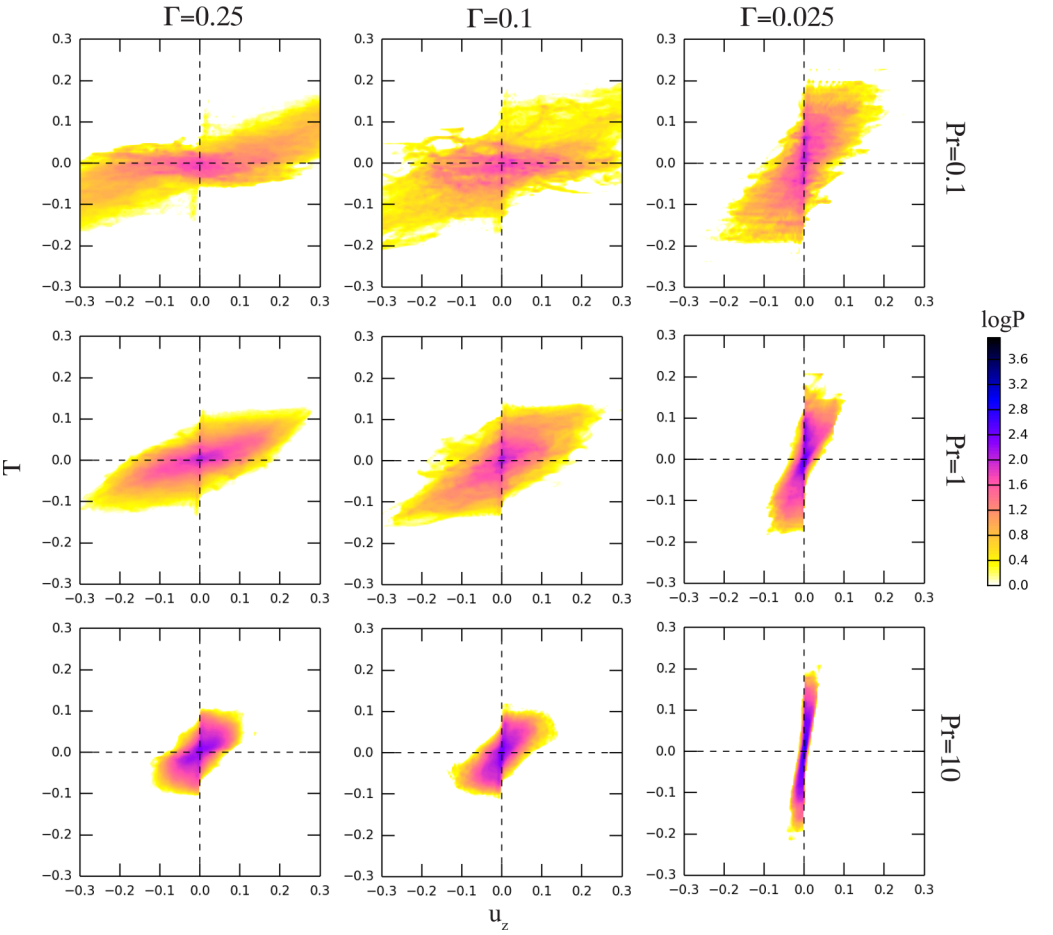

FIG. 5. Joint probability density function for the temperature T and vertical velocity u_z (both are dimensionless) evaluated at midheight for Pr $= 0.1$, 1, and 10 with $\Gamma = 0.25$, 0.1, and 0.025.

C. Physical quantities in thermal boundary layers

Figure 6(a) shows the temperature standard deviation σ_T evaluated at the edge of thermal BL versus $\Gamma/\Gamma_{\rm opt}$, where the estimation of temperature BL thickness λ_T is based on the peak location of vertical temperature standard deviation profiles $\sigma_T(z) = \sqrt{\langle T^2\rangle_{x,y,t} - \langle T\rangle^2_{x,y,t}}$. Here we normalize Γ by $\Gamma_{\rm opt}$ to better illustrate how the quantities vary as the optimal point is approached. Indeed, the local quantities taken from the thermal BL allow us to observe the differences attributed to Pr. For large Pr cases, we clearly see that σ_T increases as Γ is reduced towards $\Gamma_{\rm opt}$. Also worth noting is that the trend is more pronounced for the few largest values of Pr. This may be understood by recognizing that larger Pr corresponds to smaller thermal diffusivity and so the plumes are able to better preserve their heat content when traversing to the opposite end. Conversely, for too large thermal diffusivity, i.e., the cases of Pr $= 0.1$ and 0.2, the plumes most severely lose their heat content to the ambient fluid. Thus, we do not observe an appreciable increase of σ_T at the thermal BL for those cases.

In addition, plume coverage is also important in characterizing heat transport enhancement by confinement as revealed in Refs. [22,23]. The estimation of plume coverage requires the extraction of cold (hot) plumes over the hot bottom (cold top) BL and is defined as the area satisfying $\pm(T - \langle T\rangle_{x,y}) \geqslant c\sigma_{T,0}$. Here $\sigma_{T,0}$ is the common threshold for the same Pr, which is $\sigma_T(z = \lambda_T)$ for $\Gamma = 0.25$. The empirical parameter c is chosen to be 0.5. We have tested different choices of c and found

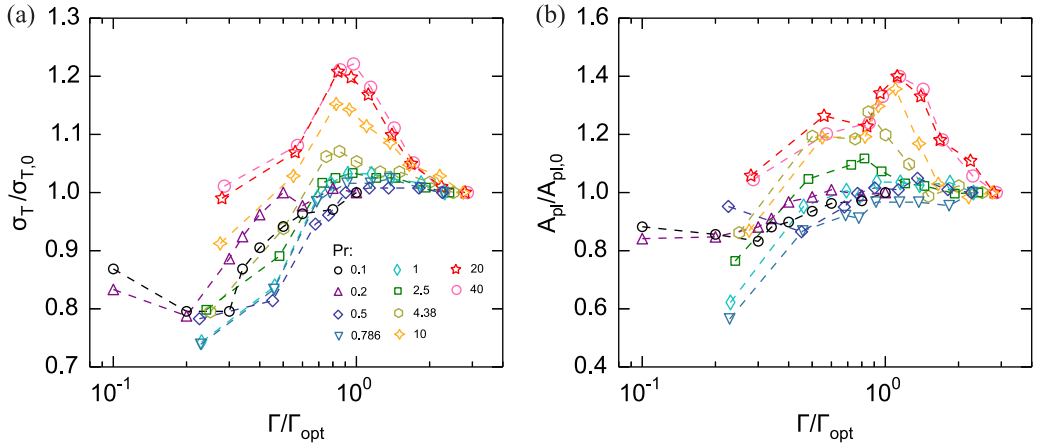

FIG. 6. (a) Temperature standard deviation σ_T evaluated at the edge of thermal BL normalized by $\sigma_{T,0}$ (obtained at $\Gamma = 0.25$ for a given Pr) versus rescaled aspect ratio $\Gamma/\Gamma_{\text{opt}}$. Note that Γ_{opt} is ill defined for $\text{Pr} = 0.1$ and 0.2 and we take $\Gamma_{\text{opt}} = 0.25$ for convenience. (b) Areal coverage of cold plumes over the edge of the (hot) bottom thermal BL A_{pl} normalized by its value obtained at $\Gamma = 0.25$ (denoted by $A_{pl,0}$) versus $\Gamma/\Gamma_{\text{opt}}$.

that our main conclusions do not depend on the particular choice of its value. Figure 6(b) shows the normalized coverage of cold plumes over the edge of the (hot) bottom thermal BL versus the rescaled aspect ratio $\Gamma/\Gamma_{\text{opt}}$. For large Pr cases, it shows clearly that, as Γ_{opt} is approached, the plume coverage is increased significantly. This suggests that the bottom (top) BL is cooled down (heated up) more efficiently, which also results in a thinner and more uniform BL [22]. Again, such an increase in plume coverage is largely absent for very low Pr, i.e., $\text{Pr} = 0.1$ and 0.2. One the whole, we see that the properties of both σ_T and plume coverage at the edge of the thermal BL can explain the behavior of the Pr dependence of Nu in response to confinement.

D. Crossing of momentum and temperature boundary layers

In a recent study [23], it has been shown that the relative thickness of thermal and momentum BLs plays a major role in determining the optimal transport. To understand the Pr-dependent optimal point found in this work, we follow the same idea. Using the proposal made by Chong *et al.* [23], the thickness λ_p of the momentum BL may be defined by the peak location of the vertical profile of the stress $s(z) = \langle(\partial_x u)^2 + (\partial_y v)^2 + (\partial_z w)^2\rangle_{x,y,t}$. The edge of the momentum BL as defined can be thought of as the location where plume merging and convolution take place such that the strongest convergence of fluid element gives rise to the maximum normal stress. Figure 7(a) shows the normalized momentum BL thickness versus the rescaled aspect ratio $\Gamma/\Gamma_{\text{opt}}$ for different Pr. First, for $\text{Pr} \geqslant 0.5$, we observe that the momentum BL becomes thinner as Γ is reduced towards Γ_{opt}. The amount of decline in thickness increases with Pr. Specially, a 20% decrease is seen for $\text{Pr} = 0.5$ and a 50% decrease for $\text{Pr} = 40$. In contrast, such a decrease is absent for the cases of $\text{Pr} = 0.1$ and 0.2. We next examine the ratio of the thicknesses of the thermal and momentum BLs λ_T/λ_p versus $\Gamma/\Gamma_{\text{opt}}$, which is presented in Fig. 7(b). It is found that the ratio of BLs thicknesses generally increases with decreasing Γ for $\text{Pr} \geqslant 0.5$ but again, not for $\text{Pr} = 0.1$ and 0.2. At a certain $\Gamma/\Gamma_{\text{opt}}$ close to one, the thermal and momentum BLs have comparable thickness such that the location of the maximum normal stress coincides with that of maximum temperature fluctuation. This BLs crossing leads to the strongest coupling of normal stress and temperature fluctuation, which is a favorable condition for plume emission [23]. However, when the confinement becomes too severe, the momentum BL will be nested deeply inside the thermal one. Previous works have shown that temperature fluctuations decrease sharply within the thermal BL [53,54]. Therefore, when the momentum BL becomes much

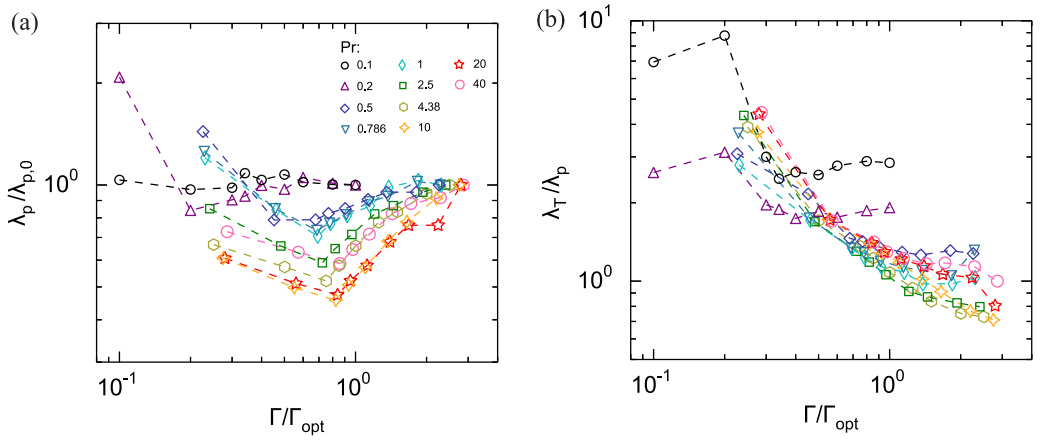

FIG. 7. (a) Momentum boundary layer thickness λ_p normalized by $\lambda_{p,0}$, the one obtained at $\Gamma = 0.25$ for a given Pr, versus rescaled aspect ratio $\Gamma/\Gamma_{\text{opt}}$. (b) Ratio of the temperature boundary layer thickness to the momentum one λ_T/λ_p versus $\Gamma/\Gamma_{\text{opt}}$.

thinner than the thermal BL, the convergence of fluid will occur at positions of much-reduced thermal instability and thus is not favorable for plume emission and heat transport. To provide evidence of such coupling, we have examined the normalized temperature standard deviation at the edge of momentum BL $\sigma_T/\sigma_{T,0}$ versus thickness ratio λ_T/λ_p as shown in Fig. 8(a). When the momentum BL becomes thinner and approaches the thickness of the thermal BL, an increase of σ_T at the edge of the momentum BL is observed. However, when the thickness ratio becomes much larger than one, σ_T drops sharply. As the figure suggests, BL crossing entails the strongest coupling between the normal stress and temperature standard deviation that is crucial to heat transport. To further demonstrate this, we plot Nu against the thickness ratio in Fig. 8(b). It can be seen that the optimal transport occurs for a thickness ratio around one, namely, between 1.08 and 1.32 (the shaded strip), and it again justifies that the BL crossing is intimately related to the optimal point.

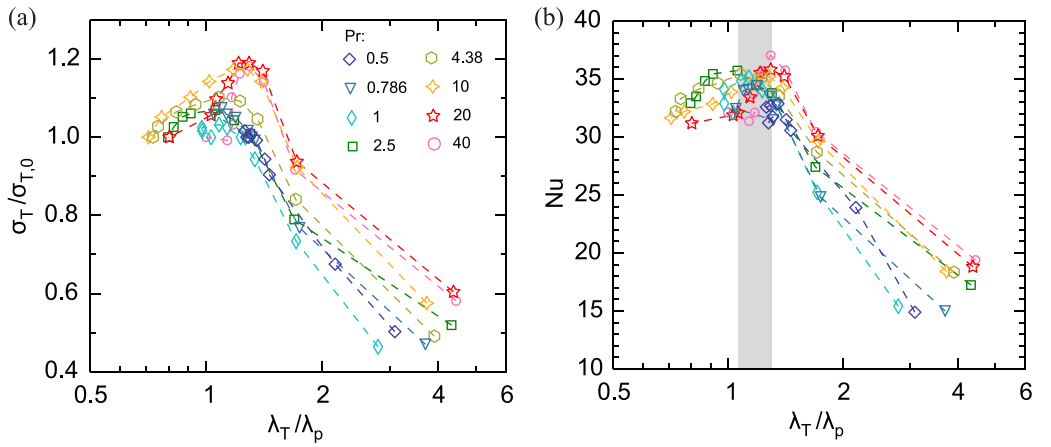

FIG. 8. (a) Normalized temperature standard deviation $\sigma_T/\sigma_{T,0}$ versus thickness ratio λ_T/λ_p, where σ_T is evaluated at the edge of momentum BL. (b) Nusselt number Nu versus λ_T/λ_p.

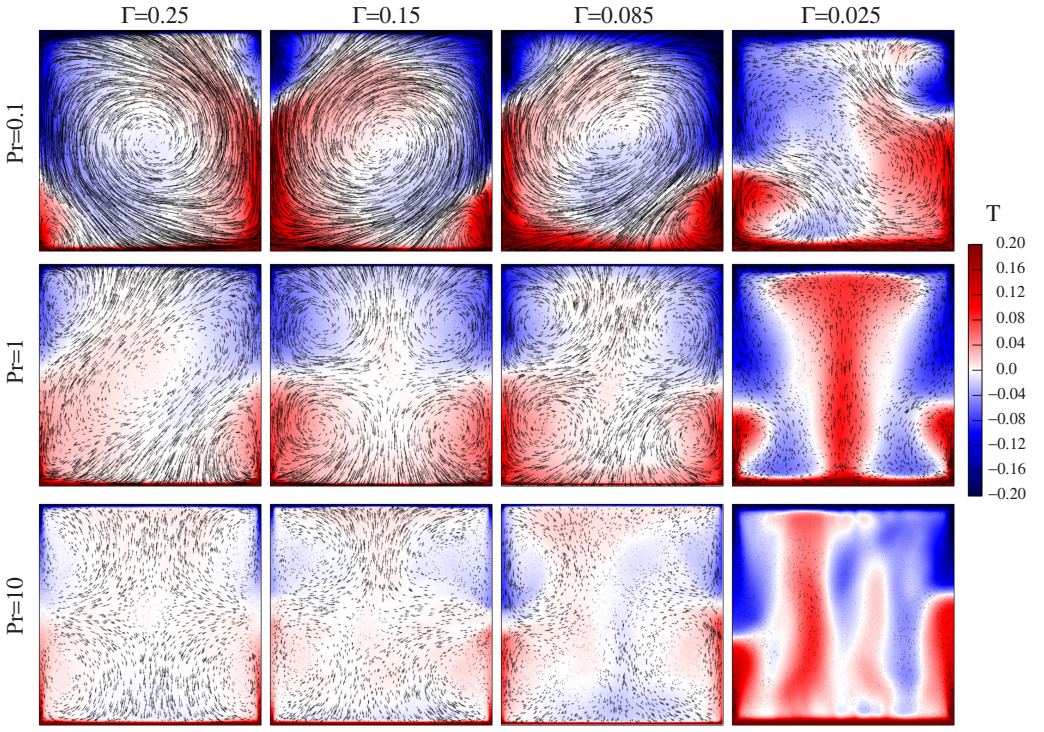

FIG. 9. Time-averaged temperature and velocity fields midway along the confinement direction for three different Pr, which are Pr = 0.1, 1, and 10, and for four different Γ, which are Γ = 0.25, 0.15, 0.085, and 0.025. The magnitude of the velocity is represented by the length of the arrows in nondimensional units and the temperature is coded in color.

E. Global flow structures

We now examine the changes in flow pattern brought about by confinement for fluid with different Pr. Figure 9 displays temporally averaged mean velocity fields along the x-z plane at midwidth together with temperature fields. We illustrate the properties of the mean flow field using four different Γ (0.25, 0.15, 0.085, and 0.025, from left to right) and three different Pr (0.1, 1 and 10, from top to bottom). We first consider the case of Pr = 0.1 and Γ = 0.25. It demonstrates a typical flow pattern in RB convection where there exists a well-defined LSC with two counterrotating corner rolls. For such a case, plumes most likely detach near sidewalls; therefore, hot and cold regions form on either side of the cell and the mean temperature field provides such a footprint. Due to the existence of corner rolls, plumes no longer impinge the opposite plates head on but rather at an angle as they are being steered. As Γ decreases to Γ = 0.15 and further to 0.085, besides the reduced flow speed, the shape change of LSC is observed. As the figure suggests, the size of the LSC shrinks while the two corner rolls grow under confinement. With further confinement to Γ = 0.025, the shape of LSC becomes greatly distorted and impingement of plumes becomes head on.

With Pr increased to 1, the variation of the flow pattern under confinement exhibits a different behavior. For Γ = 0.25 at this Pr, the LSC still persists, but larger corner rolls are seen as compared to the cases with Pr = 0.1. However, when Γ is further reduced to 0.15, the mean field displays a four-roll pattern as opposed to a single-roll flow structure. Some earlier studies had revealed that a time-averaged four-roll pattern can be brought about by the superposition of two flow fields with opposite flow directions [44,55]. The change of flow pattern indicates that the LSC becomes less stable and therefore flow reversals occur more frequently. Upon further confinement to Γ = 0.085,

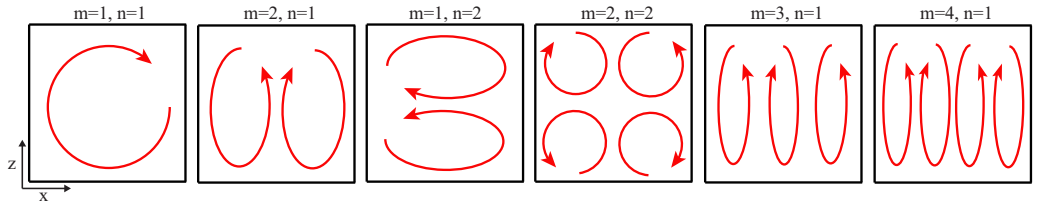

FIG. 10. Schematic diagram of the 2D Fourier modes $u_x^{m,n}$ and $u_z^{m,n}$ as defined in the text.

the four-roll flow pattern still persists. However, when Γ reaches 0.025, the flow becomes dominated by vertical motions such that columnar structures appear in the temperature field. For $\mathrm{Pr} = 10$, the single-roll structure has already broken down to a four-roll one at $\Gamma = 0.25$. This demonstrates that the LSC under confinement becomes less stable for larger Pr. Upon further confinement to $\Gamma = 0.025$, the flow field again exhibits the formation of columnar plumes and vertically aligned structures.

A more quantitative approach to study the flow pattern and strength of LSC is via the so-called 2D mode decomposition method [29,56,57]. We remark that this 2D technique is suitable here because our configurations are quasi-2D and the circulations are largely within the x-z plane. We apply the decomposition algorithm to a set of vertical cross sections from instantaneous flow fields taken at midwidth, with the planar velocity field (u_x, u_z) being projections into the Fourier modes given as

$$u_x^{m,n} = 2\sin(m\pi x)\cos(n\pi z), \tag{4}$$

$$u_z^{m,n} = -2\cos(m\pi x)\sin(n\pi z). \tag{5}$$

Usually, the first four modes are considered [29,57], i.e., $m,n \in \{1,2\}$, but now, we also consider the modes of $m = 3$ and $n = 1$ and of $m = 4$ and $n = 1$ to represent the columnar structure as found in the mean field. To give an impression of how these modes look like, we draw their corresponding flow patterns in Fig. 10. As suggested in Ref. [29], the projection is done componentwise on individual snapshots such that the time series of $A_x^{m,n}(t) = \langle u_x(t) u_x^{m,n} \rangle_{x,z}$ and $A_z^{m,n}(t) = \langle u_z(t) u_z^{m,n} \rangle_{x,z}$ are obtained. Then a value $M^{m,n}$ representing the mode contribution can be evaluated by $M^{m,n} = \langle \sqrt{(A_x^{m,n})^2 + (A_z^{m,n})^2} \rangle_t$.

In Fig. 11 we compare the contributions of each mode $M^{m,n}$ as a function of Γ for different Pr. Similar to the mean field, we have chosen $\mathrm{Pr} = 0.1$, 1, and 10 for demonstration. First we consider $\mathrm{Pr} = 0.1$ at $\Gamma = 0.25$. The value of $M^{1,1}$, which represents the single-roll structure, is at least 4 times larger than that of other modes. Upon decreasing Γ, the first mode $M^{1,1}$ becomes less dominant over other modes but is still the largest one. When Γ reaches about 0.075, $M^{1,1}$ declines sharply and becomes comparable to $M^{2,2}$, which represents the four-roll structure. From the discussion in the preceding section, this is an indication that the LSC is being suppressed by confinement. When

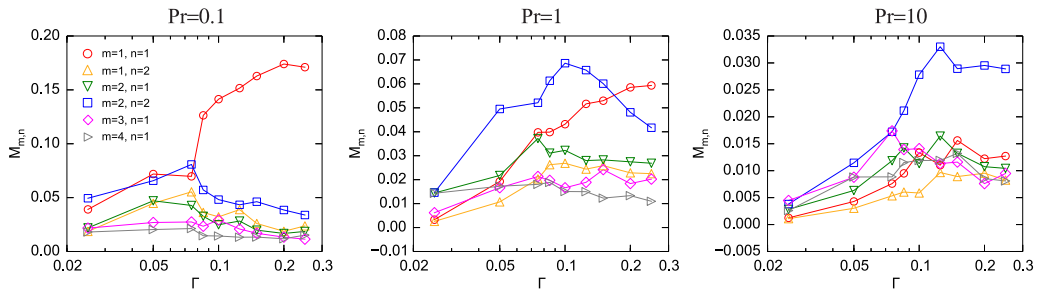

FIG. 11. Magnitudes of the four 2D modes $M^{m,n}$ as a function of the aspect ratio Γ for $\mathrm{Pr} = 0.1$, 1, and 10.

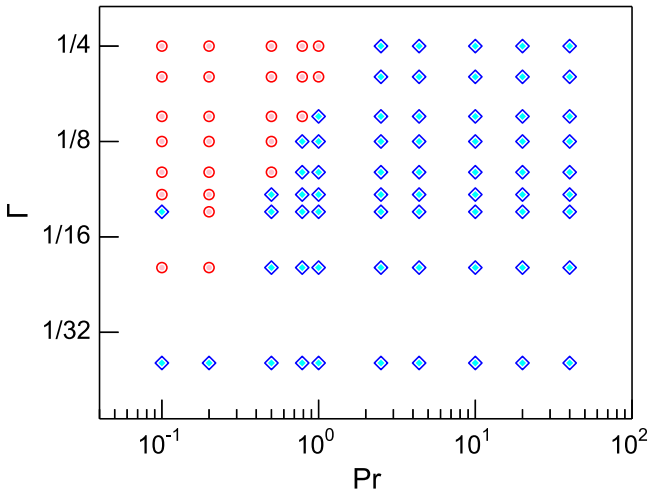

FIG. 12. Phase diagram showing the existence of the LSC in the Γ-Pr parameter space. Red circles represent cases where the value of $M^{1,1}$ (single-roll mode) is the largest compared to the other three modes; otherwise, the cases are represented by blue diamonds.

confinement is increased further to $\Gamma = 0.025$, the magnitudes of $M^{1,1}$ and $M^{2,2}$ remain comparable to each other. For $\mathrm{Pr} = 1$, $M^{1,1}$ is still the mode with the largest magnitude at $\Gamma = 0.25$ but its value is only 1.5 times larger than that of others. The most prominent feature here is that the $M^{2,2}$ mode overtakes the $M^{1,1}$ mode below $\Gamma = 0.15$, indicating the formation of a four-roll flow pattern. Our quantitative result again demonstrates that the LSC is less stable for larger Pr. The mode $M^{2,2}$ dominates until $\Gamma = 0.025$, where $M^{2,1}$ and $M^{4,1}$ become comparable to $M^{2,2}$, which could indicate the formation of vertically aligned flow structures. For $\mathrm{Pr} = 10$, the mode $M^{2,2}$ dominates until $\Gamma = 0.075$, where $M^{3,1}$ begins to have comparable magnitude to $M^{2,2}$. It again demonstrates the formation of columns for highly confined RB. This method enables us to quantify the strength of LSC and judge the presence of LSC by considering whether $M^{1,1}$ is the largest mode among others. Figure 12 gives the phase diagram illustrating when to expect the existence of LSC in the Γ-Pr parameter space.

IV. CONCLUSION

We have studied the role played by the Prandtl number Pr in geometrical confinement in terms of its effect on heat transport and flow structures, through DNS with $0.1 \leqslant \mathrm{Pr} \leqslant 40$, $0.025 \leqslant \Gamma \leqslant 0.25$, and Ra fixed at 10^8. With regard to global convective heat transport, it was found that the existence, and the amount, of heat transport enhancement brought about by confinement depends strongly on Pr. For $\mathrm{Pr} \geqslant 0.5$, significant heat transport enhancement has been observed but not for $\mathrm{Pr} = 0.1$ and 0.2. We were able to define an optimal aspect ratio Γ_{opt} at which Nu is maximized for cases with enhancement. The Pr dependence of Γ_{opt} was found to follow a power-law relationship $\Gamma_{\mathrm{opt}} = 0.11\,\mathrm{Pr}^{-0.060\pm0.004}$. Together with the result $\Gamma_{\mathrm{opt}} = 29.37\,\mathrm{Ra}^{0.31}$ found in Ref. [22], they present a more complete picture of geometrical confinement. With regard to the amount of enhancement, the maximum enhancement generally increases with Pr over the explored parameter range, ranging from 5.3% to 15.3% as Pr increased from 0.5 to 40 (for $\mathrm{Ra} = 10^8$, as the maximum enhancement also depends on Ra). Through the joint probability density function between vertical velocity and temperature standard deviations at midheight, we were able to identify two competing effects due to confinement. On the one hand, confinement reduces the flow strength; on the other hand, plumes become more coherent as revealed by the temperature distribution function. However, compared to these bulk properties, local

quantities at the edge of thermal BL including plume coverage and temperature standard deviation were found to play more important roles in determining the global heat transport. It helps us to understand why larger Pr produces larger enhancement and why no enhancement is observed for smaller values of Pr, such as 0.1 and 0.2. To explain Γ_{opt}, we have examined the relative thickness of thermal and momentum BLs λ_T/λ_p. It was suggested in Ref. [23] that the BL thickness ratio near unity actually corresponds to the situation with strongest coupling between the normal stress and the temperature fluctuations. This optimal coupling between the two quantities leads to the optimal transport. Our results with different Pr at $\mathrm{Ra} = 10^8$ support this physical picture and again justify that optimal transport occurs when λ_T/λ_p is around one. We have in addition studied the global flow structure by examining the temporally averaged flow fields and through a 2D mode decomposition. A consequence of the geometrical confinement is the weakening of LSC, which is manifested by the fact that the single-roll flow structure is replaced by a multiple-roll structure in the time-averaged flow field. It is also supported by results from the 2D mode decomposition that the $M^{1,1}$ mode no longer dominates. We further show that the LSC persists over a wider range of Γ for smaller Pr. A phase diagram for the LSC existence is shown in Fig. 12. In the future, it would also be interesting to extend the present study to Ra beyond 10^8 in a way to complete the parameter space of $\mathrm{Nu}(\mathrm{Ra},\mathrm{Pr},\Gamma)$. In addition to being of fundamental interest, those results would also be useful for passive thermal management.

ACKNOWLEDGMENTS

This work was conducted under the Cooperation Agreement between the Max Planck Society and the Chinese University of Hong Kong. It was supported by the Hong Kong Research Grants Council under Project No. CUHK1430115, CUHK Direct Grant No. 3132740, and NSFC/RGC Joint Research Grant No. N_CUHK437/15 and through a Hong Kong Ph.D. Fellowship. O.S. and S.W. thank German Research Foundation for the support under Grants No. Sh 405/3 and No. Sh 405/4, Heisenberg Fellowship, and the Priority Programme SPP 1881 "Turbulent Superstructures." The authors are also grateful for the support of computational resources by the Leibniz-Rechenzentrum (LRZ) under Project No. pr84pu.

[1] F. H. Busse, Differential rotation in steller convection zones, Astrophys. J. **159**, 629 (1970).
[2] J. C. Wyngaard, Atmospheric turbulence, Annu. Rev. Fluid Mech. **24**, 205 (1992).
[3] P. F. Linden, The fluid mechanics of natural ventilation, Annu. Rev. Fluid Mech. **31**, 201 (1999).
[4] O. Shishkina and C. Wagner, A numerical study of turbulent mixed convection in an enclosure with heated rectangular elements, J. Turbul. **13**, N22 (2012).
[5] J. Bailon-Cuba, O. Shishkina, C. Wagner, and J. Schumacher, Low-dimensional model of turbulent mixed convection in a complex domain, Phys. Fluids **24**, 107101 (2012).
[6] G. Ahlers, S. Grossmann, and D. Lohse, Heat transfer and large-scale dynamics in turbulent Rayleigh-Bénard convection, Rev. Mod. Phys. **81**, 503 (2009).
[7] D. Lohse and K.-Q. Xia, Small-scale properties of turbulent Rayleigh-Bénard convection, Annu. Rev. Fluid Mech. **42**, 335 (2010).
[8] F. Chillà and J. Schumacher, New perspectives in turbulent Rayleigh-Bénard convection, Eur. Phys. J. E **35**, 58 (2012).
[9] K.-Q. Xia, Current trends and future directions in turbulent thermal convection, Theor. Appl. Mech. Lett. **3**, 052001 (2013).
[10] Y. Shen, P. Tong, and K.-Q. Xia, Turbulent Convection Over Rough Surfaces, Phys. Rev. Lett. **76**, 908 (1996).

[11] Y.-B. Du and P. Tong, Enhanced Heat Transport in Turbulent Convection Over a Rough Surface, Phys. Rev. Lett. **81**, 987 (1998).
[12] P. Wei, T.-S. Chan, R. Ni, X.-Z. Zhao, and K. Q. Xia, Heat transport properties of plates with smooth and rough surfaces in turbulent thermal convection, J. Fluid Mech. **740**, 28 (2014).
[13] S. Wagner and O. Shishkina, Heat flux enhancement by regular surface roughness in turbulent thermal convection, J. Fluid Mech. **763**, 109 (2015).
[14] Y.-C. Xie and K.-Q. Xia, Turbulent thermal convection over rough plates with varying roughness geometries, J. Fluid Mech. **825**, 573 (2017).
[15] G. Ahlers and A. Nikolaenko, Effect of a Polymer Additive on Heat Transport in Turbulent Rayleigh-Bénard Convection, Phys. Rev. Lett. **104**, 034503 (2010).
[16] R. Benzi, E. S. C. Ching, and E. De Angelis, Effect of Polymer Additives on Heat Transport in Turbulent Thermal Convection, Phys. Rev. Lett. **104**, 024502 (2010).
[17] P. Wei, R. Ni, and K.-Q. Xia, Enhanced and reduced heat transport in turbulent thermal convection with polymer additives, Phys. Rev. E **86**, 016325 (2012).
[18] R. Benzi, E. S. C. Ching, and V. W. S. Chu, Heat transport by laminar boundary layer flow with polymers, J. Fluid Mech. **696**, 330 (2012).
[19] Y.-C. Xie, S.-D. Huang, D. Funfschilling, X.-M. Li, R. Ni, and K.-Q. Xia, Effects of polymer additives in the bulk of turbulent thermal convection, J. Fluid Mech. **784**, R3 (2015).
[20] S.-D. Huang, M. Kaczorowski, R. Ni, and K.-Q. Xia, Confinement-Induced Heat-Transport Enhancement in Turbulent Thermal Convection, Phys. Rev. Lett. **111**, 104501 (2013).
[21] S. Horn and O. Shishkina, Rotating non-Oberbeck-Boussinesq Rayleigh-Bénard convection in water, Phys. Fluids **26**, 055111 (2014).
[22] K. L. Chong, S. D. Huang, M. Kaczorowski, and K. Q. Xia, Condensation of Coherent Structures in Turbulent Flows, Phys. Rev. Lett. **115**, 264503 (2015).
[23] K. L. Chong, Y. Yang, S.-D. Huang, J.-Q. Zhong, R. J. A. M. Stevens, R. Verzicco, D. Lohse, and K.-Q. Xia, Confined Rayleigh-Bénard, Rotating Rayleigh-Bénard, and Double Diffusive Convection: A Unifying View on Turbulent Transport Enhancement through Coherent Structure Manipulation, Phys. Rev. Lett. **119**, 064501 (2017).
[24] S. Grossmann and D. Lohse, On geometry effects in Rayleigh-Bénard convection, J. Fluid Mech. **486**, 105 (2003).
[25] E. S. C. Ching and W. S. Tam, Aspect-ratio dependence of heat transport by turbulent Rayleigh-Bénard convection, J. Turbul. **7**, N72 (2006).
[26] J. Bailon-Cuba, M. S. Emran, and J. Schumacher, Aspect ratio dependence of heat transfer and large-scale flow in turbulent convection, J. Fluid Mech. **655**, 152 (2010).
[27] E. P. van der Poel, R. J. A. M. Stevens, K. Sugiyama, and D. Lohse, Flow states in two-dimensional Rayleigh-Bénard convection as a function of aspect-ratio and Rayleigh number, Phys. Fluids **24**, 085104 (2012).
[28] Q. Zhou, B.-F. Liu, C.-M. Li, and B.-C. Zhong, Aspect ratio dependence of heat transport by turbulent Rayleigh-Bénard convection in rectangular cells, J. Fluid Mech. **710**, 260 (2012).
[29] S. Wagner and O. Shishkina, Aspect-ratio dependency of Rayleigh-Bénard convection in box-shaped containers, Phys. Fluids **25**, 085110 (2013).
[30] K. L. Chong and K. Q. Xia, Exploring the severely confined regime in Rayleigh-Bénard convection, J. Fluid Mech. **805**, R4 (2016).
[31] S. Cioni, S. Ciliberto, and J. Sommeria, Strongly turbulent Rayleigh-Bénard convection in mercury: Comparison with results at moderate Prandtl number, J. Fluid Mech. **335**, 111 (1997).
[32] E. Brown, A. Nikolaenko, and G. Ahlers, Reorientation of the Large-Scale Circulation in Turbulent Rayleigh-Bénard Convection, Phys. Rev. Lett. **95**, 084503 (2005).
[33] C. Sun, H.-D. Xi, and K.-Q. Xia, Azimuthal Symmetry, Flow Dynamics, and Heat Transport in Turbulent Thermal Convection in a Cylinder with an Aspect Ratio of 0.5, Phys. Rev. Lett. **95**, 074502 (2005).
[34] H.-D. Xi, Q. Zhou, and K.-Q. Xia, Azimuthal motion of the mean wind in turbulent thermal convection, Phys. Rev. E **73**, 056312 (2006).

[35] D. Funfschilling, E. Brown, A. Nikolaenko, and G. Ahlers, Heat transport by turbulent Rayleigh-Bénard convection in cylindrical cells with aspect ratio one and larger, J. Fluid Mech. **536**, 145 (2005).
[36] C. Sun, L.-Y. Ren, H. Song, and K.-Q. Xia, Heat transport by turbulent Rayleigh-Bénard convection in cylindrical cells of widely varying aspect ratios, J. Fluid Mech. **542**, 165 (2005).
[37] K.-Q. Xia, C. Sun, and Y.-H. Cheung, Large scale velocity structures in turbulent thermal convection with widely varying aspect ratio, *Proceedings of the 14th International Symposium on Applications of Laser Techniques to Fluid Mechanics, Lisbon, 2008*.
[38] H.-D. Xi and K.-Q. Xia, Flow mode transitions in turbulent thermal convection, Phys. Fluids **20**, 055104 (2008).
[39] H.-D. Xi and K.-Q. Xia, Azimuthal motion, reorientation, cessation, and reversal of the large-scale circulation in turbulent thermal convection: A comparative study in aspect ratio one and one-half geometries, Phys. Rev. E **78**, 036326 (2008).
[40] R. Ni, S.-D. Huang, and K.-Q. Xia, Reversals of the large-scale circulation in quasi-2D Rayleigh-Bénard convection, J. Fluid Mech. **778**, R5 (2015).
[41] S.-D. Huang and K.-Q. Xia, Effects of geometric confinement in quasi-2-D turbulent Rayleigh-Bénard convection, J. Fluid Mech. **794**, 639 (2016).
[42] O. Shishkina and S. Wagner, Prandtl-Number Dependence of Heat Transport in Laminar Horizontal Convection, Phys. Rev. Lett. **116**, 024302 (2016).
[43] M. Kaczorowski and K.-Q. Xia, Turbulent flow in the bulk of Rayleigh-Bénard convection: Small-scale properties in a cubic cell, J. Fluid Mech. **722**, 596 (2013).
[44] M. Kaczorowski, K.-L. Chong, and K.-Q. Xia, Turbulent flow in the bulk of Rayleigh-Bénard convection: Aspect-ratio dependence of the small-scale properties, J. Fluid Mech. **747**, 73 (2014).
[45] M. Kaczorowski, A. Shishkin, O. Shishkina, and C. Wagner, Developement of a numerical procedure for direct simulations of turbulent convection in a closed rectangular cell, in *New Results in Numerical and Experimental Fluid Mechanics VI*, edited by C. Tropea, S. Jakirlic, H. J. Heinemann, R. Henke, and H. Hönlinger (Springer, Berlin, 2007), Vol. 96, pp. 381–388.
[46] O. Shishkina, R. J. A. M Stevens, S. Grossmann, and D. Lohse, Boundary layer structure in turbulent thermal convection and its consequences for the required numerical resolution, New J. Phys. **12**, 075022 (2010).
[47] S. Grossmann and D. Lohse, Scaling in thermal convection: A unifying theory, J. Fluid Mech. **407**, 27 (2000).
[48] B. I. Shraiman and E. D. Siggia, Heat transport in high-Rayleigh-number convection, Phys. Rev. A **42**, 3650 (1990).
[49] R. J. A. M. Stevens, E. P. van der Poel, S. Grossmann, and D. Lohse, The unifying theory of scaling in thermal convection: The updated prefactors, J. Fluid Mech. **730**, 295 (2013).
[50] K.-Q. Xia, S. Lam, and S.-Q Zhou, Heat-Flux Measurement in High-Prandtl-Number Turbulent Rayleigh-Bénard Convection, Phys. Rev. Lett. **88**, 064501 (2002).
[51] S. Grossmann and D. Lohse, Thermal Convection for Large Prandtl Numbers, Phys. Rev. Lett. **86**, 3316 (2001).
[52] O. Shishkina, M. S. Emran, S. Grossmann, and D. Lohse, Scaling relations in large-Prandtl-number natural thermal convection, Phys. Rev. Fluids **2**, 103502 (2017).
[53] A. Belmonte, A. Tilgner, and A. Libchaber, Temperature and velocity boundary layers in turbulent convection, Phys. Rev. E **50**, 269 (1994).
[54] S.-L. Lui and K.-Q. Xia, Spatial structure of the thermal boundary layer in turbulent convection, Phys. Rev. E **57**, 5494 (1998).
[55] C. Sun, K.-Q. Xia, and P. Tong, Three-dimensional flow structures and dynamics of turbulent thermal convection in a cylindrical cell, Phys. Rev. E **72**, 026302 (2005).
[56] K. Petschel, M. Wilczek, M. Breuer, R. Friedrich, and U. Hansen, Statistical analysis of global wind dynamics in vigorous Rayleigh-Bénard convection, Phys. Rev. E **84**, 026309 (2011).
[57] M. Chandra and M. K. Verma, Dynamics and symmetries of flow reversals in turbulent convection, Phys. Rev. E **83**, 067303 (2011).